Advanced x-ray diagnostics based on an observation of high-energy Rydberg transitions from autoionizing levels in dense laser-produced plasmas

F. B. Rosmej, D. H. H. Hoffmann, M. Geißel, M. Roth, and P. Pirzadeh
GSI-Darmstadt, Institute of Plasma Physics, Planckstrasse 1, D-64220 Darmstadt, Germany and Technische Universität Darmstadt, Institute of Nuclear Physics, Schloßgartenstrasse 9, D-64289 Darmstadt, Germany

A. Ya. Faenov, T. A. Pikuz, I. Yu. Skobelev, and A. I. Magunov
Multicharged Ions Spectra Data Center of VNIIFTRI, Russian Committee of Standards, Mendeleevo, 141570 Moscow Region, Russia
(Received 22 September 2000; published 15 May 2001)

The application of x-ray spectroscopy methods enabled a space-resolved observation of the high-energy Rydberg satellite series $1s2lnl' \rightarrow 1s^2 2l + h\nu$ and the Ly_β satellites $2l3l' \rightarrow 1s2l + h\nu$ in dense laser-produced plasmas. *Ab initio* atomic structure calculations including relativistic and QED effects show excellent agreement with the precise wavelengths measurements. Satellite transitions with $n>3$ split into three distinct groups. For $n>5$, the transitions are found to merge with the Ly_β satellite transitions $2l3l' \rightarrow 1s2l + h\nu$ and the series limits approach the Ly_β line. This leads to emission on the red and even on the blue wing of the Ly_β line. Spatially and spectrally resolved intensity distribution discovered strong spatial restrictions of the Rydberg satellite intensities near the target surface. On the contrary, all resonance lines show strong emissions up to 10-mm distance from the target and large optical thickness. This enabled us to develop essentially opacity-free and spatially localized temperature diagnostics based on Rydberg satellite emission. Total x-ray emission spectra are established with the help of the MARIA suite of kinetic codes. The derived properties of the spectral distribution make the high-energy Rydberg satellites of general interest for the wide class of dense plasma experiments.

DOI: 10.1103/PhysRevA.63.063409 PACS number(s): 32.80.Dz, 32.70.Fw, 32.30.Rj

I. INTRODUCTION

Line transitions from autoionizing states are very important for diagnostics. Since the early work of Gabriel [1], they have historically been employed for sensitive temperature determination of astrophysical plasmas. However, the application to dense hot plasmas, such as, e.g., inertial confinement fusion plasmas, laser-produced plasmas or pinching plasmas, is not straightforward due to opacity, non-Maxwellian electrons, inhomogeneity, and transient effects. The advanced development of dielectronic satellite models [2–17] has created a new interest in these transitions also for dense plasma experiments and resulted in many applications to inertial confinement fusion in hohlraums [18], laser-produced plasmas [6,11,14,19,20], and pinching plasmas [10,12,13,17,21].

However, it was pointed out [22–25] that serious opacity effects may even occur for transitions from autoionizing states. Unlike usual resonance line emission, opacity in dielectronic satellites changes dramatically the intensity and spectral distribution because high autoionizing rates (of order $10^{14}\,\mathrm{s}^{-1}$) act like depopulating collisions from upper levels [22]. As autoionizing rates decrease rapidly with the principal quantum number n, opacity results in a complete distortion of the emission spectrum. Examples of complete distortions have been observed recently in laser-produced plasmas: high opacity led to the disappearance of resonance line emission and the accumulation of Rydberg satellites near the resonance line position [24–27].

It is obvious that sophisticated modeling is indispensable to obtain diagnostic information from optically thick spectra. In real experiments, however, opacity is often accompanied by inhomogeneities. Even for space-resolved spectroscopic arrangements, line-of-sight integrations are unavoidable. This introduces large uncertainties for the interpretation.

All this indicates that there is an urgent need to develop methods for diagnostics that are intrinsically based on optically thin emission lines with small line-of-sight integration effects. Generally speaking, opacity problems can be excluded by using transitions caused by radiative decay of highly excited Rydberg levels. In order to maintain the great diagnostic advantages of satellite transitions, transitions from autoionizing Rydberg levels are therefore highly desirable. These transitions, however, are not established yet for dense plasmas.

Therefore, to develop methods for plasma diagnostics based on Rydberg satellites requires, as a first step, identifying these transitions in experimental spectra, measuring their wavelengths, and comparing experimental data with atomic structure calculations. The second step is to perform kinetic calculations to obtain the spectral distribution in order to derive diagnostic sensitivities.

Both tasks are solved in the present paper for the case of Rydberg satellites caused by transitions from autoionizing levels $1s2lnl'$ of Li-like Si XII. Atomic structure calculations take into account relativistic and QED effects for high-n transitions until the series limits are established. Based on these investigations, kinetic modeling is established and diagnostic properties are derived from the spectral distribution.

Moreover, we also address the important phenomena related to inhomogeneous emission. For these purposes, highly

advanced x-ray optical methods have been installed at the GSI nhelix-laser test bed facility in Darmstadt. These methods employ high luminosity focusing x-ray spectrographs providing simultaneously high spectral and spatial resolution. We show that, in particular, resonance line emissions and dielectronic satellites show up with quite different spatial emission sizes: Rydberg-satellite emission appeared to be spatially very narrow. Based on these findings, methods to address directly local emission zones are developed.

Finally, essentially opacity-free space-resolved temperature diagnostic methods are developed and demonstrated in the present paper. The results are of general interest for the large class of dense plasma experiments and significantly advance the spectroscopic analyses.

II. EXPERIMENTAL SETUP

Dense plasmas have been created at GSI with the 100-J nhelix-laser facility irradiating massive Si targets. nhelix is a Nd-glass–YAG (YAG denotes yttrium aluminum garnet) laser operating at a wavelength of $\lambda = 1.064$ μm and a pulse width of 15 ns. A focusing lens with 100-mm diam and 150-mm focal length was used. Targets were irradiated with 30 J and spot sizes of about 100–500 μm.

Space-solved x-ray spectra were recorded with spherically bent mica crystals [28–30] in third order with a curvature radius of $R = 150$ mm. The central Bragg angle was $\theta_0 = 35°$, the distance between target and x-ray film (Kodak DEF V x-ray film with grain size less than 2 μm) was $a = 280$ mm, and between crystal and film was $b = 136$ mm. In order to protect the film from visible light, two polypropylene foils with a thickness of 2 μm each covered with 0.1-μm Al from each side were used. An additional polypropylene foil without Al cover was used for a debris shield.

Plasma images were digitized with 5000 dpi (dots per inch) employing a EUROCORE 10.000 dpi drum scanner. This arrangement enabled a spatial resolution in the z direction (z is the direction of the expanding plasma perpendicular to the target surface) of $(0.0254\ \text{m}/5000)(280/136)/\cos 35° = 12.8$ μm per pixel and a spectral resolution of about $\lambda/\delta\lambda \approx 3500$. Spectra have been corrected for filter transmissions, crystal reflectivity, film response, and nonlinear dispersion scale (using He_ζ, He_γ resonance lines and the He_β intercombination line as reference lines) using the program SCALE.

Figure 1(a) shows the soft-x-ray plasma image in the very broad wavelength interval ranging from 0.51 to 0.57 nm containing the resonance lines $1snp\ ^1P_1 \rightarrow 1s^2\ ^1S_0 + h\nu$ from $n = 3$ until the series limit. Distinct line emission until $n = 11$ was observed. The horizontal dark line corresponds to the emission near the target surface (bremsstrahlung), and above, the recombination regime of the resonance lines is seen with emissions up to about 10 mm from the target surface. Figures 1(b) and 1(c) show corresponding traces taken at different target distances (we note that all intensity scales are linear).

III. THE IDENTIFICATION OF HIGH-ENERGY RYDBERG SATELLITE EMISSION, WAVELENGTH MEASUREMENTS, AND ATOMIC STRUCTURE CALCULATIONS

The spectrum taken near the target surface [Figs. 1(b) and 1(c)] shows (apart from the usual He-like resonance lines)

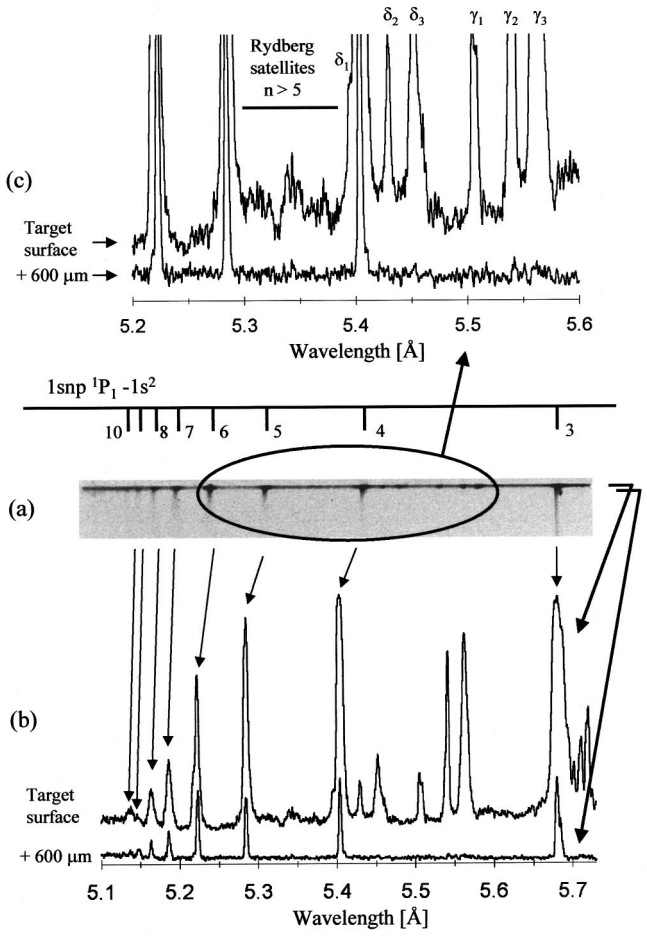

FIG. 1. Space-resolved plasma image (a) of silicon K-shell x-ray line emission obtained at the GSI nhelix-laser installation. Indicated are the He-like resonance lines until the series limit as well as the high-energy Rydberg satellites $1s2lnl' \rightarrow 1s^2 2l + h\nu$. Two spectra are shown: first, from the target surface [strong black horizontal line in (a)] showing strong emissions of dielectronic satellites (resolved satellite groups $\gamma_1, \gamma_2, \gamma_3, \delta_1, \delta_2, \delta_3$ are considered in Table I); second, in the expanding plasma (taken 600 μm above the surface). The total emission size of the He_β resonance line is observable up to 10 mm.

also strong emissions between the $\text{He}_\delta = 1s5p\ ^1P_1 \rightarrow 1s^2\ ^1S_0 + h\nu$ and $\text{He}_\gamma = 1s4p\ ^1P_1 \rightarrow 1s^2\ ^1S_0 + h\nu$ lines. Sophisticated atomic structure calculations identify these transitions as high-energy Rydberg dielectronic satellite transitions:

$$1s2lnl' \rightarrow 1s^2 2l + h\nu_{\text{sat}}.$$

The corresponding low-energy transitions

$$1s2lnl' \rightarrow 1s^2 nl' + h\nu_{\text{sat}}$$

give rise to the satellite near He_α. In laser-produced plasmas, these satellites constitute the main intensity near the He_α line [19,24,25].

High-energy Rydberg satellite data are, however, not very well established. We therefore have undertaken extended numerical calculations based on the multiconfiguration

TABLE I. Atomic data and measured wavelengths λ_e of Li-like silicon high-energy Rydberg satellites $1s2lnl' \rightarrow 1s^2 2l + h\nu_{sat}$ for $n=4,5$. The present theoretical calculations (wavelengths λ_t, transition probabilities A, and satellite intensity factors Q) were carried out with the multiconfiguration Z-expansion method including higher-order relativistic and QED effects.

Key	Transition	λ_t (10^{-10} m)	λ_e (10^{-10} m)	A (s)	Q (s)
		$n=5$			
δ_1	$1s2s[^1S]5p\ ^2P_{3/2}-1s^2 2s\ ^2S_{1/2}$	5.3953	5.3959(5)	1.5×10^{11}	5.7×10^{11}
	$1s2s[^1S]5p\ ^2P_{1/2}-1s^2 2s\ ^2S_{1/2}$	5.3959		3.8×10^{11}	7.0×10^{11}
δ_2	$1s2s[^3S]5p\ ^2P_{1/2}-1s^2 2s\ ^2S_{1/2}$	5.4313	5.4301(5)	1.4×10^{12}	1.5×10^{12}
	$1s2s[^3S]5p\ ^2P_{3/2}-1s^2 2s\ ^2S_{1/2}$	5.4313		1.4×10^{12}	3.1×10^{12}
δ_3	$1s2p[^3P]5p\ ^2D_{3/2}-1s^2 2p\ ^2P_{1/2}$	5.4517	5.4523(5)	5.3×10^{11}	1.8×10^{12}
	$1s2p[^3P]5p\ ^2D_{5/2}-1s^2 2p\ ^2P_{3/2}$	5.4526		8.4×10^{11}	4.6×10^{12}
		$n=4$			
γ_1	$1s2s[^1S]4p\ ^2P_{3/2}-1s^2 2s\ ^2S_{1/2}$	5.5044	5.5050(5)	3.3×10^{11}	1.3×10^{12}
	$1s2s[^1S]4p\ ^2P_{1/2}-1s^2 2s\ ^2S_{1/2}$	5.5055		5.1×10^{11}	9.4×10^{11}
	$1s2p[^3P]4s\ ^2P_{3/2}-1s^2 2s\ ^2S_{1/2}$	5.5094	5.5091(5)	7.7×10^{11}	4.6×10^{11}
	$1s2p[^3P]4s\ ^2P_{1/2}-1s^2 2s\ ^2S_{1/2}$	5.5106		6.2×10^{11}	7.7×10^{11}
γ_2	$1s2p[^1P]4p\ ^2D_{5/2}-1s^2 2p\ ^2P_{3/2}$	5.5412	5.5428(5)	7.6×10^{11}	1.3×10^{12}
	$1s2s[^3S]4p\ ^2P_{1/2}-1s^2 2s\ ^2S_{1/2}$	5.5427		2.6×10^{12}	2.5×10^{12}
	$1s2s[^3S]4p\ ^2P_{3/2}-1s^2 2s\ ^2S_{1/2}$	5.5428		2.6×10^{12}	5.1×10^{12}
γ_3	$1s2p[^3P]5p\ ^2S_{1/2}-1s^2 2p\ ^2P_{3/2}$	5.5595	5.5591(5)	2.3×10^{12}	2.1×10^{12}
	$1s2p[^3P]4p\ ^2D_{3/2}-1s^2 2p\ ^2P_{1/2}$	5.5617	5.5617(5)	2.1×10^{12}	7.0×10^{12}
	$1s2p[^3P]4p\ ^2D_{5/2}-1s^2 2p\ ^2P_{3/2}$	5.5623		2.3×10^{12}	1.2×10^{13}
	$1s2s[^1S]4d\ ^2D_{5/2}-1s^2 2p\ ^2P_{3/2}$	5.5630	5.5641(5)	6.3×10^{11}	3.0×10^{12}
	$1s2p[^3P]4p\ ^2D_{3/2}-1s^2 2p\ ^2P_{3/2}$	5.5643		8.7×10^{11}	2.9×10^{12}

Z-expansion method including the relativistic energy shift due to contact terms and orbit-orbit interaction (defined by the Breit operator), relativistic term splitting connected with spin-orbit and spin-spin interaction, and Lamb shift correction including vacuum polarization [31–35]. Corresponding atomic data and experimental wavelengths are depicted in Table I. The data show that for $n>3$, the satellites $1s2lnl'-1s^2 2l$ separate into three distinct emission peaks even in high-resolution spectra ($\lambda/\delta\lambda\approx4000$). The key indicates satellites that accumulate to these three groups. It can be seen from Table I that almost all satellite wavelengths agree within 1 mÅ between the calculations and the measurements. It should be noted that all theoretical data are *ab initio* calculations and neither groups nor single lines have been shifted. The table presents also the spontaneous radiative decay rate A and the dielectronic satellite intensity factor

$$Q=\frac{g_s}{g_\Gamma}\frac{A\Gamma}{\Sigma A+\Gamma}. \tag{1}$$

g_s and g_Γ are the statistical weights of the autoionizing level and the state from which autoionization proceeds, Γ is the autoionizing rate, and the sum is taken over all possible channels of radiative and autoionization decay. The satellite intensity factor determines the dielectronic recombination-rate coefficient (in units of $cm^3\,s^{-1}$)

$$\langle R_D\rangle=\alpha Q\frac{\exp(-E_s/kT_e)}{(kT_e)^{3/2}}. \tag{2}$$

E_s is the capture energy in eV, kT_e is the electron temperature in eV, and $\alpha=1.656\times10^{-22}\ cm^3\,s^{-1}$. For large Q factors, the dielectronic recombination rate provides an estimate to the expected intensity.

Figures 1(b) and 1(c) also show a spectrum taken 600 μm above the target. It is seen that at this distance almost all satellite transitions have disappeared. Figure 2 compares the different emission zones of the He_δ line, the He_δ satellites, as well as the bremsstrahlung from the target surface. It is clearly seen that the full width at half maximum (FWHM) of

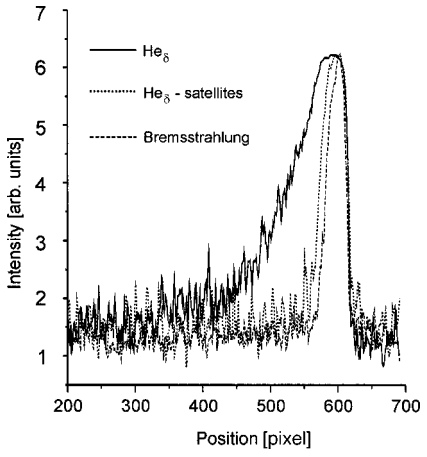

FIG. 2. Spatial emission zones of the He_δ, the He_δ satellites, and the bremsstrahlung. The satellite emission peaks in a very narrow spatial interval.

the He_δ emission is 98 pixels (corresponding to 1.3 mm). Also, a strong wing extending to about 300 pixels (3.8 mm) is seen for the He_δ emission, whereas the satellite emission extends to only 46 pixels (590 μm). The comparison with the narrowest emission size, namely the bremsstrahlung (note that this dimension defines approximately the smallest emission size defined by the laser spot size) from the target surface with 34 pixels (440 μm), shows that the high-energy Rydberg transitions are spatially very well localized.

These properties are very favorable for diagnostics. If the line intensity by itself is localized in a very narrow spatial interval, line-of-sight integration effects (which always persist even in space-resolved spectra) are negligible. The opposite behavior is seen for the resonance lines. Their emission extends over large spatial intervals; see the wing structure of He_δ in Fig. 2.

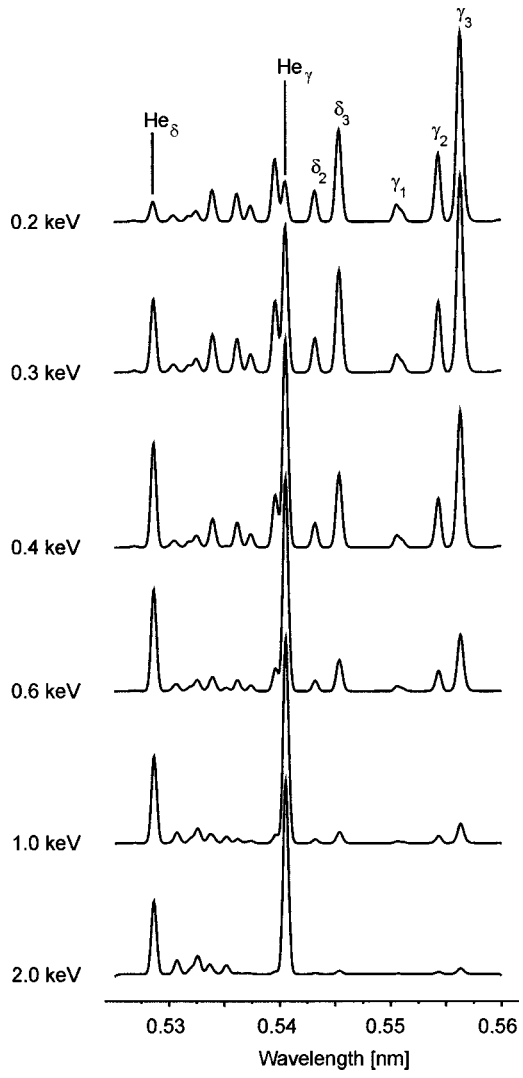

FIG. 3. Essentially opacity-free temperature sensitivity is obtained employing He_γ and He_δ Rydberg-satellite transitions. MARIA simulation parameters are $n_e = 10^{20}$ cm^{-3} and $L_{\rm eff} = 100$ μm.

TABLE II. Line-center opacities τ_0 of various transitions for an electron temperature of (a) $kT_e = 300$ eV, $n_e = 10^{20}$ cm^{-3}, and $L_{\rm eff} = 100$ μm; (b) $kT_e = 300$ eV, $n_e = 10^{21}$ cm^{-3}, and $L_{\rm eff} = 500$ μm [e.g., $O(-3)$ means that τ_0 is of the order of 10^{-3}].

	τ_0							
Transitions	He_α	He_β	He_γ	He_δ	He_α-sat.	He_β-sat.	He_γ-sat.	He_δ-sat.
(a)	21	3.9	1.4	0.61	$O(-2)$	$O(-2)$	$O(-3)$	$O(-3)$
(b)	980	170	50	16	$O(1)$	$O(-1)$	$O(-2)$	$O(-2)$

IV. ADVANCED DIAGNOSTIC EMPLOYING OPACITY-FREE RYDBERG SATELLITES

The most effective method to study the diagnostic properties of a large number of transitions with possible line overlapping is via spectra simulations. We employ the MARIA suite of codes [15] to perform multilevel collisional radiative opacity calculations and subsequent spectra simulations. The upper level densities n_j are determined from a system of rate equations,

$$\frac{dn_j}{dt} = \sum_{i \neq j} n_i \{W_{ij} + A_{ij}\Lambda_{ij}\} - n_j \sum_{k \neq j} \{W_{jk} + A_{jk}\Lambda_{jk}\}. \quad (3)$$

The matrix W is given by

$$W_{ij} = C_{ij} + C_{p_{ij}} + R_{ij} + I_{ij} + I_{p_{ij}} + T_{ij} + \Gamma_{ij} + C_{D_{ij}}. \quad (4)$$

C is the collisional excitation/deexcitation matrix, I the collisional ionization matrix, T the three-body recombination, R the radiative recombination, Γ the autoionization, C_D the dielectronic capture, A the spontaneous radiative decay matrix, and ion-ion (atom) collisions (excitation/deexcitation and ionization) are described by the matrixes C_p and I_p. The

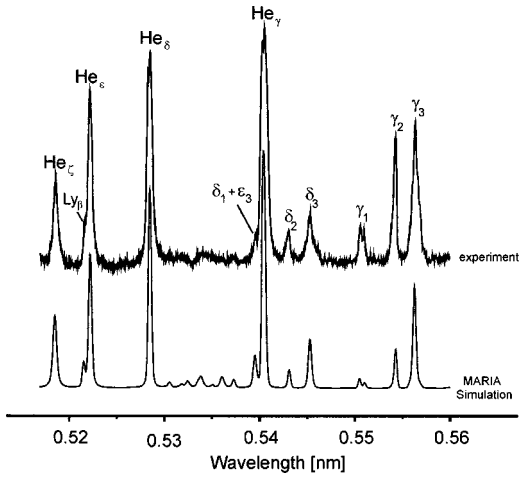

FIG. 4. Comparison of the experimental spectrum and the MARIA simulations in the spectral interval from the He_ζ until the γ_3 satellites. Excellent agreement with the line positions and quite good overall agreement are seen. Simulation parameters are $kT_e = 350$ eV, $n_e = 10^{21}$ cm^{-3}, $L_{\rm eff} = 100$ μm, and $\lambda/\delta\lambda_{\rm instrument} \approx 3500$.

TABLE III. Atomic data and measured wavelengths λ_e (or line overlapping) of Li-like silicon high-energy Rydberg satellite $1s2lnl' \rightarrow 1s^2 2l + h\nu_{sat}$. Higher-order Rydberg-satellite groups show strong overlapping with each other and with the Ly_β satellites (see Fig. 3). Line identification was accomplished with the MARIA spectral simulations. (Other notation as in Table I.)

Key	Transition	λ_t (10^{-10} m)	λ_e (10^{-10} m)	A (s)	Q (s)
		$n=15$			
ξ_1	$1s2s[^1S]15p\ ^2P_{3/2}-1s^22s\ ^2S_{1/2}$	5.2332		1.7×10^{10}	3.1×10^{10}
	$1s2s[^1S]15p\ ^2P_{1/2}-1s^22s\ ^2S_{1/2}$	5.2332		1.5×10^{10}	5.2×10^{10}
ξ_2	$1s2s[^3S]15p\ ^2P_{1/2}-1s^22s\ ^2S_{1/2}$	5.2670	5.2662	5.0×10^{10}	6.2×10^{10}
	$1s2s[^3S]15p\ ^2P_{3/2}-1s^22s\ ^2S_{1/2}$	5.2670		5.0×10^{10}	1.2×10^{11}
ξ_3	$1s2p[^3P]15p\ ^2D_{3/2}-1s^22p\ ^2P_{1/2}$	5.2884	Blended by	3.6×10^{10}	7.5×10^{10}
	$1s2p[^3P]15p\ ^2D_{5/2}-1s^22p\ ^2P_{3/2}$	5.2887	He_δ	4.0×10^{10}	2.2×10^{11}
		$n=9$			
θ_1	$1s2s[^1S]9p\ ^2P_{3/2}-1s^22s\ ^2S_{1/2}$	5.2680	5.2674	4.5×10^{10}	1.7×10^{11}
	$1s2s[^1S]9p\ ^2P_{1/2}-1s^22s\ ^2S_{1/2}$	5.2682		7.9×10^{10}	1.5×10^{11}
θ_2	$1s2s[^3S]9p\ ^2P_{1/2}-1s^22s\ ^2S_{1/2}$	5.3023	5.3012[a]	2.3×10^{11}	2.9×10^{11}
	$1s2s[^3S]9p\ ^2P_{3/2}-1s^22s\ ^2S_{1/2}$	5.3023		2.3×10^{11}	5.7×10^{11}
θ_3	$1s2p[^3P]9p\ ^2D_{3/2}-1s^22p\ ^2P_{1/2}$	5.3239	5.3238[a]	1.9×10^{11}	6.0×10^{11}
	$1s2p[^3p]9p\ ^2D_{5/2}-1s^22p\ ^2P_{3/2}$	5.3241		1.9×10^{11}	1.0×10^{12}
		$n=8$			
η_1	$1s2s[^1S]8p\ ^2P_{3/2}-1s^22s\ ^2S_{1/2}$	5.2827	Blended by	6.8×10^{10}	2.7×10^{11}
	$1s2s[^1S]8p\ ^2P_{1/2}-1s^22s\ ^2S_{1/2}$	5.2829	He_δ	1.1×10^{11}	2.1×10^{11}
η_2	$1s2s[^3S]8p\ ^2P_{1/2}-1s^22s\ ^2S_{1/2}$	5.3172	5.3170	3.3×10^{11}	4.1×10^{11}
	$1s2s[^3S]8p\ ^2P_{3/2}-1s^22s\ ^2S_{1/2}$	5.3172		3.3×10^{11}	8.1×10^{11}
η_3	$1s2p[^3P]8p\ ^2D_{3/2}-1s^22p\ ^2P_{1/2}$	5.3388	5.3395(7)	2.9×10^{11}	9.1×10^{12}
	$1s2p[^3P]8p\ ^2D_{5/2}-1s^22p\ ^2P_{3/2}$	5.3390		2.6×10^{11}	1.4×10^{12}
		$n=7$			
ζ_1	$1s2s[^1S]7p\ ^2P_{3/2}-1s^22s\ ^2S_{1/2}$	5.3043	5.3043[a]	1.1×10^{11}	4.1×10^{11}
	$1s2s[^1S]7p\ ^2P_{1/2}-1s^22s\ ^2S_{1/2}$	5.3046		1.6×10^{11}	3.0×10^{11}
ζ_2	$1s2s[^3S]7p\ ^2P_{1/2}-1s^22s\ ^2S_{1/2}$	5.3391	5.3395(7)	5.0×10^{11}	6.0×10^{11}
	$1s2s[^3S]7p\ ^2P_{3/2}-1s^22s\ ^2S_{1/2}$	5.3391		5.0×10^{11}	1.2×10^{12}
ζ_3	$1s2p[^3P]7p\ ^2D_{3/2}-1s^22p\ ^2P_{1/2}$	5.3608	5.3602(7)	4.4×10^{11}	1.4×10^{12}
	$1s2p[^3P]7p\ ^2D_{5/2}-1s^22p\ ^2P_{3/2}$	5.3609		3.4×10^{11}	1.9×10^{12}
		$n=6$			
ε_1	$1s2s[^1S]6p\ ^2P_{3/2}-1s^22s\ ^2S_{1/2}$	5.3380	5.3391	1.6×10^{11}	6.3×10^{11}
	$1s2s[^1S]6p\ ^2P_{1/2}-1s^22s\ ^2S_{1/2}$	5.3385		2.0×10^{11}	3.6×10^{11}
ε_2	$1s2s[^3S]6p\ ^2P_{1/2}-1s^22s\ ^2S_{1/2}$	5.3733	5.3726(7)	7.9×10^{11}	9.3×10^{11}
	$1s2s[^3S]6p\ ^2P_{3/2}-1s^22s\ ^2S_{1/2}$	5.3733		7.9×10^{11}	1.9×10^{12}
ε_3	$1s2p[^3P]6p\ ^2D_{3/2}-1s^22p\ ^2P_{1/2}$	5.3951	5.3959	6.8×10^{11}	2.1×10^{12}
	$1s2p[^3P]6p\ ^2D_{5/2}-1s^22p\ ^2P_{3/2}$	5.3950		4.7×10^{11}	2.6×10^{12}

[a]Blended by Ly_β satellites.

indices ''*ij*'' indicate the transition from level ''*i*'' to level ''*j*''; if a matrix element physically does not exist, its value is zero. The radiation terms are contained in $\Lambda(L_{\rm eff})$, where $L_{\rm eff}$ is the effective photon path length [36]. For optically thick plasmas, the set of differential equations becomes nonlinear, because $\Lambda_{ij}=\Lambda_{ij}(n_i,n_j)$. The level system chosen includes all the Si ground states (nucleus until neutral Si), H-like levels nl with $n=1-7$ and $l=0-6$, He-like levels $1snl$ with $n=1-7$, $l=0-6$, Li-like levels $1s^2nl$ with $n=2-7$, $l=0-6$, as well as effective dielectronic and radiative recombination rates for all charge states. Also included are all dipole allowed ($\Delta S=0$) and intercombination ($\Delta S=1$) transitions from the autoionizing states $2lnl'$ with $n=2-4$, $1s2lnl'$ with $n=2-9$.

Figure 3 shows simulated spectra in the wavelength interval from 0.525 until 0.560 nm for different electron temperatures ($kT_e=0.2-2$ keV). A large sensitivity to the electron temperature over one order of magnitude is seen for the He_δ and He_γ satellites δ_2, δ_3, γ_1, γ_2, and γ_3, respectively. Moreover, these transitions have favorable properties against opacity. Table II depicts the line-center opacities τ_0,

$$\tau_0=\tfrac{1}{4}\lambda_{ji}^2\frac{g_j}{g_i}A_{ji}n_i\left\{1-\frac{g_in_j}{g_jn_i}\right\}\varphi_{ij}(\omega=\omega_{ji})L_{\rm eff} \qquad (5)$$

(λ is the wavelength, g_j and g_i are the statistical weights of the upper and lower level respectively, n_i is the density of the absorbing ground state, and φ is the absorption profile), of various resonance lines and satellites for different parameters: (a) $kT_e=300$ eV, $n_e=10^{20}$ cm^{-3}, and $L_{\rm eff}=100$ μm; (b) $kT_e=300$ eV, $n_e=10^{21}$ cm^{-3}, and $L_{\rm eff}=500$ μm. He_α and He_β have a line-center optical thickness of several hundred and even the He_α satellites are optically thick. In contrast, He_γ and He_δ lines show moderate opacities and entirely optically thin satellite structure.

Figure 4 shows the application of the above-developed Rydberg-satellite temperature diagnostic to the present data. Comparing the upper (experiment) and lower (MARIA simulation) spectrum, quite good overall agreement is seen for $kT_e\approx 350$ eV. It should be emphasized that this procedure is highly advanced because, first, spatially restricted emission data are analyzed and, second, entirely low or opacity-free transitions are taken. This method is therefore of general interest for dense plasma experiments such as, e.g., laser-produced plasmas and pinch plasmas.

V. Ly_β SATELLITES AND THE Li-LIKE HIGH-ENERGY RYDBERG SATELLITE SERIES LIMITS

Next, we consider the Rydberg-satellite transitions up to the series limit, which have not been observed in dense laser-produced plasmas so far. Table III shows the present atomic data calculations for Rydberg satellites to He_ε ($n=6$), He_ζ ($n=7$), He_η ($n=8$), He_θ ($n=9$), and He_ξ ($n=15$) for the three groups of lines. Figure 5 shows the spectra simulations. We present spectra simulations with different contributions to show the very details: (a) the satellites to He_δ, He_ε, and He_ζ; (b) to He_η and He_θ. One can see that transitions of all Rydberg satellites split again into three main groups. These groups are located far from their corresponding resonance lines and accumulate mainly near the spectral interval of He_δ and He_γ. Starting with $n=5$, these three groups show serious line overlapping.

Figure 5(c) shows that the line overlapping is not only determined by the Rydberg satellites itself but also by the satellite transitions

$$2l3l' \rightarrow 1s2l + h\nu_{\rm sat}.$$

Ly_β is the corresponding resonance line. Table IV shows the series limits of the three Li-like satellite groups. It can be seen clearly that the Li-like high-energy Rydberg-satellite groups 2 and 3 approach the Ly_β line [central wavelength of $\lambda(\mathrm{Ly}_\beta)=5.217$ Å] and group 1 is located even on the blue wavelengths side of the Ly_β line.

The establishment of these series limits may have very important consequences for the interpretation of emission peaks near the Ly_β line of highly charged ions. These peaks have been previously proposed to be due to plasma satellites [37] and molecular satellites [38], whereas these works [37,38] did not consider the Rydberg-satellite emission of the present work.

To our knowledge, the upper spectrum in Fig. 6 shows the first observation of space-resolved Rydberg satellites with

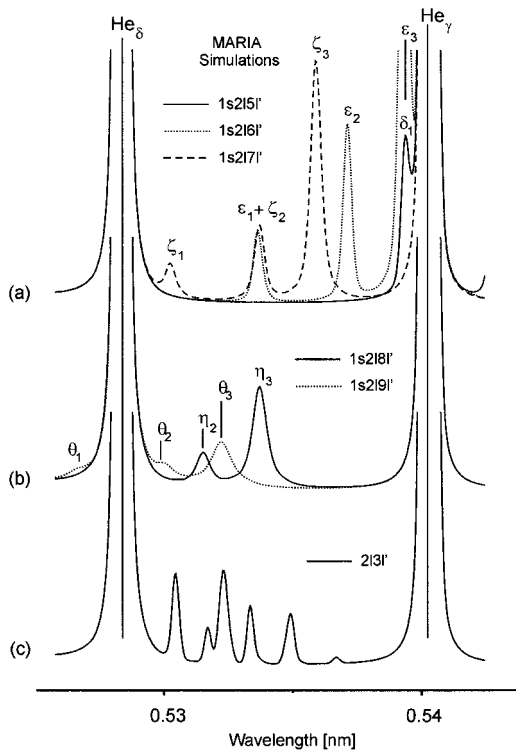

FIG. 5. Simulations showing the different contributions from the dielectronic satellite spectra with the Li-like high-energy transitions $1s2lnl' \rightarrow 1s^2 2l + h\nu$ and the He-like Ly_β satellites $2lnl' \rightarrow 1s2l + h\nu$: (a) contributions for $n=5,6,7$; (b) $n=8,9$; and (c) spectral distribution of the Ly_β satellite spectra. Designations are defined in Tables I and III.

$n>5$ in dense laser-produced plasmas. The lower spectrum shows the MARIA simulation. Good overall agreement is obtained for the same simulation parameters as obtained above (Fig. 4). Obviously very many emission peaks coincide (see vertical bars).

The established Rydberg-satellite transition series are also proposed for advanced Stark broadening analysis exhibiting the unique property of negligible opacity and spatial restriction. Although the autoionizing configurations are rather complex, Stark broadening calculations will be feasible in the near future [39] and the present data provide experimental information on this issue, too.

VI. CONCLUSION

We have observed space-resolved Li-like silicon high-energy Rydberg satellite transitions until the series limit in

TABLE IV. Series limits of the satellite groups ''1,'' ''2,'' and ''3'' for a Si XII ion.

Satellite group	Series limit
1	5.213×10^{-10} m
2	5.247×10^{-10} m
3	5.269×10^{-10} m

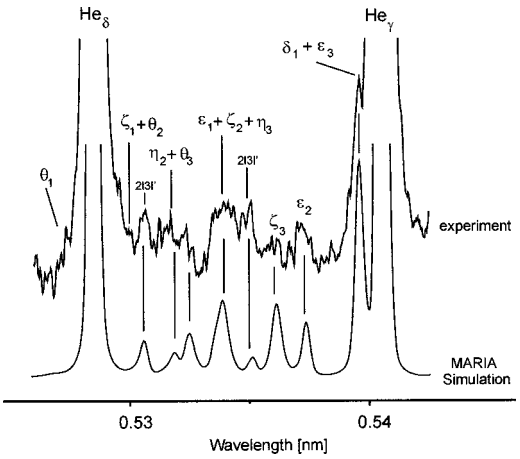

FIG. 6. Expanded scale of the Rydberg-satellite spectrum. Quite good agreement between the experimental (upper spectrum) and the MARIA simulation (lower spectrum) is seen when including the Li-like Rydberg satellites as well as the Ly$_\beta$ dielectronic satellites.

dense laser-produced plasmas. Satellites to He$_\gamma$ and higher series members split into three distinct observable groups, in excellent agreement with atomic-structure calculations including relativistic and QED effects. These groups effectively radiate only in a very narrow spatial interval near the target surface and are shown to be suitable for Stark broadening analysis. The emission therefore serves as a local diagnostic probe for temperature and density, and these properties lead to a significant improvement over common diagnostic methods because high-energy Rydberg satellites are essentially optically thin even in large-scale dense plasmas.

The satellite series limits are shown to give rise to emissions at the blue and red wing of Ly$_\beta$ based on the dielectronic recombination mechanism, which is different from previously proposed mechanisms such as plasma satellites or molecular satellites.

The established data and methods of Rydberg satellites are therefore of general interest and widely applicable for dense plasma experiments. A detailed demonstration of the methods was carried out for dense silicon high-energy laser-produced plasmas.

ACKNOWLEDGMENTS

The authors are very grateful to Professor U. I. Safronova and Professor L. A. Vainshtein for long-term fruitful discussions and for making available to us their multiconfiguration *Z*-expansion code.

[1] A. H. Gabriel, Mon. Not. R. Astron. Soc. **160**, 99 (1972).
[2] A. V. Vinogradov, I. Yu. Skobelev, and E. A. Yukov, Zh. Eksp. Teor. Fiz. **72**, 1762 (1977) [Sov. Phys. JETP **45**, 925 (1977)].
[3] A. H. Gabriel and K. J. H., Mon. Not. R. Astron. Soc. **189**, 319 (1979).
[4] V. J. Jacobs and M. Blaha, Phys. Rev. A **21**, 525 (1980).
[5] A. S. Shlyaptseva, A. M. Urnov, and A. V. Vinogradov (unpublished).
[6] J. P. Matte, J. C. Kieffer, S. Ethier, and M. Chaker, Phys. Rev. Lett. **72**, 1208 (1984).
[7] M. K. Inal, J. Dubau, J. Phys. B **22**, 3329 (1989).
[8] L. A. Woltz, V. L. Jacobs, C. F. Hooper, and R. C. Mancini, Phys. Rev. A **44**, 1281 (1991).
[9] F. B. Rosmej, J. Quant. Spectrosc. Radiat. Transf. **51**, 319 (1994).
[10] O. N. Rosmej and F. B. Rosmej, in *Dense Z-Pinches*, edited by Malcolm Haines and Andrew Knight, AIP Conf. Proc. No. 299 (AIP, New York, 1994), p. 560.
[11] R. C. Mancini, P. Audebert, J. P. Geindre, A. Rousse, F. Falliès, J. C. Gauthier, A. Mysyrowicz, J. P. Chambaret, and A. Antonetti, J. Phys. B **27**, 1671 (1994).
[12] F. B. Rosmej, J. Phys. B **28**, L747 (1995).
[13] J. Abdallah, Jr., A. Ya. Faenov, D. Hammer, S. A. Pikuz, G. Csanak, and R. E. H. Clark, Phys. Scr. **53**, 705 (1996).
[14] N. C. Woolsey, A. Asfaw, B. Hammel, C. Keane, C. A. Back, A. Calisti, C. Mossé, R. Stamm, B. Talin, J. S. Wark, R. W. Lee, and L. Klein, Phys. Rev. E **53**, 6396 (1996).
[15] F. B. Rosmej, J. Phys. B **30**, L819 (1997).
[16] F. B. Rosmej and J. Abdallah, Jr., Phys. Lett. A **245**, 548 (1998).
[17] F. B. Rosmej, L. O. Baronova, V. V. Vikhrev, L. Jakubowski, M. Sadowski, O. N. Rosmej, and A. M. Urnov, J. Tech. Phys. **40**, 153 (1999).
[18] S. H. Glenzer, F. B. Rosmej, R. W. Lee, C. A. Back, K. G. Estabrook, B. J. MacCowan, T. D. Shepard, and R. E. Turner, Phys. Rev. Lett. **81**, 356 (1998).
[19] F. B. Rosmej, A. Ya. Faenov, T. A. Pikuz, F. Flora, P. Di Lazzaro, S. Bollanti, N. Lizi, T. Letardi, A. Reale, L. Palladino, O. Batani, S. Bossi, A. Bornardinello, A. Scafati, L. Reale, A. Zigler, M. Fraenkel, and R. D. Cowan, J. Quant. Spectrosc. Radiat. Transf. **58**, 859 (1997).
[20] F. B. Rosmej, D. H. H. Hoffmann, W. Süß, M. Geißel, P. Pirzadeh, M. Roth, W. Seelig, A. Ya. Faenov, I. Yu. Skobelev, A. I. Magunov, T. A. Pikuz, R. Bock, U. N. Funk, U. Neuner, S. Udrea, A. Tauschwitz, N. A. Tahir, B. Yu. Sharkov, and N. E. Andreev, JETP Lett. **70**, 270 (1999).
[21] P. Faucher, N. Peyraud-Cuenca, and F. B. Rosmej, J. Plasma Phys. **63**, 255 (2000).
[22] V. A. Boiko, S. A. Maiorov, S. A. Pikuz, I. Yu. Skobelev, A. Ya. Faenov, and K. A. Shilov, Opt. Spectrosc. **52**, 259 (1982).
[23] S. Kienle, F. B. Rosmej, and H. Schmidt, J. Phys. B **28**, 3675 (1995).
[24] F. B. Rosmej and A. Ya. Faenov, Phys. Scr. **T73**, 106 (1997).
[25] F. B. Rosmej, A. Ya. Faenov, T. A. Pikuz, I. Yu. Skobelev, A. E. Stepanov, A. N. Starostin, V. S. Rerikh, V. A. Makhrov, F. Flora, S. Bollanti, P. Di. Lazzaro, T. Letardi, K. Vigli-Papadaki, A. Nottola, A. Grilli, L. Palladino, A. Reale, A. Scafati, and L. Reale, Pis'ma Zh. Eksp. Teor. Fiz. **65**, 679 (1977) [JETP Lett. **65**, 708 (1997)].
[26] F. B. Rosmej, A. Ya. Faenov, T. A. Pikuz, F. Flora, P. Di.

Lazzaro, T. Letardi, A. Grilli, L. Reale, L. Palladino, C. Tomassetti, A. Scafati, and L. Reale, J. Phys. B **31**, L921 (1998).
[27] F. B. Rosmej, U. N. Funk, M. Geißel, D. H. H. Hoffmann, A. Tauschwitz, A. Ya. Faenov, T. A. Pikuz, I. Yu. Skobelev, F. Flora, S. Bollanti, P. Di. Lazzaro, T. Letardi, A. Grilli, L. Palladino, A. Reale, A. Scafati, L. Reale, T. Auguste, P. D'Oliveira, S. Hulin, P. Monot, A. Maksimchuk, S. A. Pikuz, D. Umstadter, M. Nantel, R. Bock, M. Dornik, M. Stetter, S. Stöwe, V. Yakushev, M. Kulisch, and N. Shilkin, J. Quant. Spectrosc. Radiat. Transf. **65**, 477 (2000).
[28] I. Yu. Skobelev, A. Ya. Faenov, B. A. Bryunetkin, and V. M. Dyakin, Zh. Eksp. Teor Fiz. **108**, 1263 (1995) [JETP **81**, 692 (1995)].
[29] B. K. F. Young *et al.*, Rev. Sci. Instrum. **69**, 4049 (1998).
[30] N. Nakamura, F. Nojikawa, H. Shiraishi, F. J. Currell, S. Ohtani, A. Ya. Faenov, and T. A. Pikuz, Rev. Sci. Instrum. **70**, 1658 (1999).
[31] L. A. Vainshtein and U. I. Safronova, At. Data Nucl. Data Tables **21**, 49 (1978).
[32] L. A. Vainshtein and U. I. Safronova, At. Data Nucl. Data Tables **25**, 311 (1980).
[33] L. A. Vainshtein and U. I. Safronova, Phys. Scr. **31**, 519 (1985).
[34] V. P. Shevelko and L. A. Vainshtein, *Atomic Physics for Hot Plasmas* (IOP, Bristol, 1993).
[35] U. I. Safronova, M. S. Safronova, and R. Bruch, J. Phys. B **28**, 2803 (1995).
[36] W. Kalkhofen, *Methods in Radiative Transfer* (Cambridge University Press, London, 1984).
[37] O. Renner, O. Peyrusse, P. Sondhaus, and E. Förster, J. Phys. B **33**, L151 (2000).
[38] P. Sauvan, E. Leboucher-Dalimer, P. Angelo, H. Derfoul, T. Ceccotti, P. Poquerusse, A. Calisti, and B. Talin, J. Quant. Spectrosc. Radiat. Transf. **65**, 511 (2000).
[39] A. Calisti (private communication).